Materials Science & Engineering A 816 (2021) 141313

Contents lists available at ScienceDirect

Materials Science & Engineering A

journal homepage: www.elsevier.com/locate/msea

Microstructure and mechanical properties of ultrafine grained CoCrFeNi and $CoCrFeNiAl_{0.3}$ high entropy alloys reinforced with Cr_2O_3/Al_2O_3 nanoparticles

Z. Zhang [a,b], Y.H. Xie [a,b], X.Y. Huo [a], S.L.I. Chan [c,d], J.M. Liang [a,b,*], Y.F. Luo [a,b], D.K.Q. Mu [a,b], J. Ju [a,b], J. Sun [e], J. Wang [a,b,**]

[a] State Key Laboratory of Metal Matrix Composites, Shanghai Jiao Tong University, 800 Dongchuan Road, Shanghai, 200240, China
[b] Shanghai Key Laboratory of Advanced High-temperature Materials and Precision Forming, Shanghai Jiao Tong University, 800 Dongchuan Road, Shanghai, 200240, China
[c] School of Materials Science and Engineering, University of New South Wales, Sydney, NSW, 2052, Australia
[d] Department of Chemical and Materials Engineering, National Central University, 300 Zhongda Road, Zhongli, 320317, Taiwan
[e] Shanghai Aerospace Equipments Manufacturer Co., Ltd., 100 Huaning Road, Shanghai, 200240, China

ARTICLE INFO

Keywords:
High entropy alloy
Ultrafine grain
Nanoparticle
Strengthening mechanism

ABSTRACT

CoCrFeNi and $CoCrFeNiAl_{0.3}$ high entropy alloys reinforced with in-situ oxide nanoparticles have been successfully fabricated by mechanical milling in combination with hot pressing and hot extrusion. The as-fabricated CoCrFeNi samples exhibited an ultrafine grained microstructure with in-situ Cr_2O_3 oxide nanoparticles formed during hot pressing and extrusion process and distributed both on grain boundaries and in grain interiors. Increasing extrusion temperature from 1000 to 1100 °C caused a significantly increase of grain size from 700 nm to 2.5 μm owing to recrystallization and growth of the recrystallized grains, as well as the coarsening of Cr_2O_3 nanoparticles with their mean size increasing from 57 to 140 nm. When adding Al elements, finer Al_2O_3 nanoparticles (mean size: 30 nm) formed in the $CoCrFeNiAl_{0.3}$ high entropy alloy, leading to refinement of the grains (mean size: 504 nm) due to their pinning effect on grain boundary immigration. After T6 heat treatment, the $CoCrFeNiAl_{0.3}$ high entropy alloy demonstrated improved mechanical properties with yield strength of 1335 MPa, ultimate tensile strength of 1346 MPa and an elongation to fracture of 7.9%. With quantitative analysis based on the current models, it was concluded that grain boundary strengthening and Orowan strengthening acted as the dominant strengthening mechanisms.

1. Introduction

High entropy alloys (HEAs) have been developed to be a novel alloy design concept to break the conventional alloy design strategy [1]. Owing to the high configurational entropy, the HEAs are endued with many specialized characteristics such as [2–4]: high entropy effect, severe lattice distortion effect, sluggish diffusion effect and cocktail effect to stabilize solid-solution phase and impede the dislocation movement, therefore they normally exhibit excellent mechanical properties. Among the HEAs, the CoCrFeNi and CoCrFeNiMn HEAs have demonstrated unprecedented strength and toughness at cryogenic temperature, attracting an increasing number of interests [5]. However, the relative low room temperature strength of these alloys restricts their potential engineering applications.

It is well recognized that the strength of an alloy can be improved significantly when refining grain size to ultrafine or nano scale owing to grain boundary strengthening. Sun et al. [6] found that the CoCrFeMnNi HEA demonstrated a significantly increase of yield strength from 225 MPa to 798 MPa when reducing the grain size from 105 μm to 650 nm. Xie et al. [7] reported an ultrafine grained CoCrFeNiMn HEA with a high yield strength of 819 MPa, and concluded that grain boundary strengthening played the most contribution to the improved strength. Shahmir et al. [8] fabricated a nanocrystalline CoCrFeNiMn HEA (average grain size: 10 nm) by high-pressure torsion. It was found that

* Corresponding author. State Key Laboratory of Metal Matrix Composites, Shanghai Jiao Tong University, 800 Dongchuan Road, Shanghai, 200240, China.
** Corresponding author. State Key Laboratory of Metal Matrix Composites, Shanghai Jiao Tong University, 800 Dongchuan Road, Shanghai, 200240, China.
E-mail addresses: jmliang@sjtu.edu.cn (J.M. Liang), Junwang@sjtu.edu.cn (J. Wang).

https://doi.org/10.1016/j.msea.2021.141313
Received 26 November 2020; Received in revised form 13 April 2021; Accepted 16 April 2021
Available online 27 April 2021

this material demonstrated a high yield strength of 1.4 GPa with elongation to fracture of 4%. Similarly, Schuh et al. [9] reported a nanocrystalline CoCrFeMnNi HEA with an ultimate tensile strength of 1950 MPa but an apparent loss of ductility due to the lack of work hardening ability [10,11].

It was reported that the ultrafine grained (UFG) and nanocrystallined (NC) structure was thermodynamically unstable due to the high grain boundary density, which brought about a high driving force for grain growth [12,13]. Kinetic stabilization by second phase dispersoids dragging the grain boundaries, which is called Zener pinning, was proposed to stable the UFG/NC structure [14]. Praveen et al. [15] synthesized NC CoCrFeNi HEA via mechanical alloying and spark plasma sintering, and found that this material demonstrated a sluggish grain growth in the annealing process at 900 °C for 600 h. They attributed this to the Zener pinning of the grain boundaries by Cr-rich carbide and oxide particles. In addition, it was believed that the dispersed particles also contribute to the increase in strength of the HEA. Xie et al. [16] added Ti and Nb into CoCrFeNiMn alloy to form dispersed Ti(C,O) and NbC particles in grain interiors. It was found that these dispersed particles could provide Orowan strengthening which is comparable to the grain boundary strengthening [16]. Liu et al. [17] introduced Nb into CoCrFeNi HEAs to form fine Laves phase in the FCC matrix, leading to an apparently increase of yield stress from 147 MPa to 637 MPa. Gwalani et al. [18] acquired B2 and σ phases in $Al_{0.3}$CoCrFeNi HEAs in various temperature based on phase diagram, and consequently increased the yield stress from 160 MPa to 1.8 GPa. However, most of the second phases are detrimental to the ductility because of their brittleness and large size. The γ′-$L1_2$ type nanoprecipitates, which have been proven to be a ductile and low-misfit coherent with FCC structured matrix such as Ni based superalloys [19], are usually used to obtain a good balance of strength and ductility. He et al. [20] fabricated the CoCrFeNi HEAs with a high density of γ′-$L1_2$ nanoprecipitates by adding Ti and Al elements via thermomechanical treatment, obtaining an increment in yield stress from 200 MPa to 1 GPa with good elongation of 17%. Similar results about good balance of strength and ductility have been demonstrated in other γ′ nanoprecipitates hardened high/medium entropy alloys [21–23].

Up to now, most of works concentrated on only one specific type of strengthening mechanism because of the difficulty in the control of microstructure containing two or above variables such as grain size, second-phase particles, precipitates, etc. Moreover, the interaction between different variables makes it a great challenge to correlate the microstructure to mechanical properties. In this study, we have successfully synthesized CoCrFeNi and $CoCrFeNiAl_{0.3}$ HEAs with microstructure consisting of UFG matrix and oxide nanoparticles by high energy ball milling in combination with hot pressing, hot extrusion and heat treatment. We also systematically controlled the variables such as grain size, oxide nanoparticles and nanoprecipitates. The purpose of this study is to investigate the evolution of microstructure and to identify the effect of each variable on mechanical properties via calculating various strengthening mechanisms.

2. Materials and methods

In this study, elemental powders of Co, Cr, Fe, Ni (purity > 99.5 wt%, mean particle size < 75 μm) were used as raw materials. The powders were firstly mixed by the planetary ball milling machine (QM-3SP4, Nanda Instrument Plant, China) with a rotation speed of 200 rpm for 6 h, and then they were milled at 300 rpm for 60 h with a ball to material weight ratio of 5:1. The milled powders were consolidated into a compact by die-pressing at 450 °C with a holding time of 5 min. The CoCrFeNi HEA compacts were heated using an induction foil to two different temperatures: 1000 °C (sample HE1000) and 1100 °C (sample HE1100). The samples were then extruded with a ratio of 9:1. The die-pressing, induction heating and extrusion were performed under an Ar protection atmosphere. The FeAl (50:50) alloy powder (purity > 99.5 wt

Table 1
Sample details and fabrication process of the CoCrFeNi and $CoCrFeNiAl_{0.3}$ HEAs.

Samples	Constitute Elements	Fabrication Process
HE1000	Co, Cr, Fe, Ni	Ball mill + Hot press + Hot extursion at 1000 °C
HE1100	Co, Cr, Fe, Ni	Ball mill + Hot press + Hot extursion at 1100 °C
AlHE1000	Co, Cr, Fe, Ni, Al	Ball mill + Hot press + Hot extursion at 1000 °C
AlHE1000HT	Co, Cr, Fe, Ni, Al	Ball mill + Hot press + Hot extursion at 1000 °C + Solution at 1150 °C + Quenching + Aging at 550 °C

Table 2
The chemical compositions (at. %) of the extruded samples.

	Co	Cr	Fe	Ni	Al
Nominal	25	25	25	25	0
HE1000	26.2	24.7	24.9	24.2	0
HE1100	25.1	25.5	25.3	24.1	0
Nominal	23.25	23.25	23.25	23.25	7
AlHE1000	23.5	23.9	22.8	22.6	7.2
AlHE1000HT	23.1	23.6	23.6	22.8	6.9

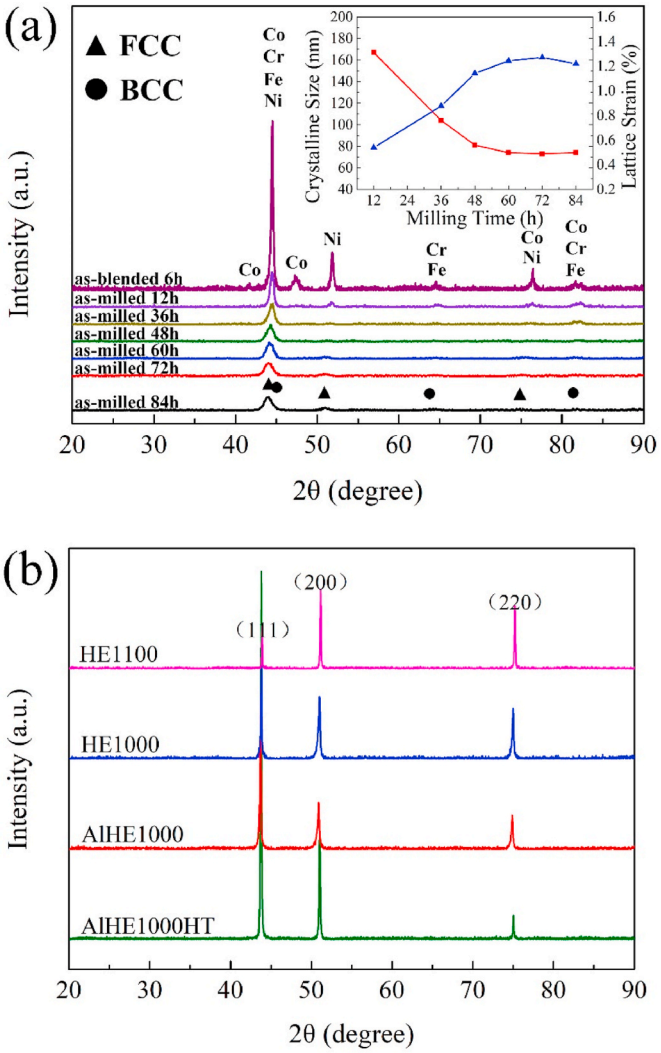

Fig. 1. X-ray diffraction patterns of (a) the mechanical milled CoCrFeNi HEA powders with different milling time and (b) the as-extruded CoCrFeNi and $CoCrFeNiAl_{0.3}$ HEA samples.

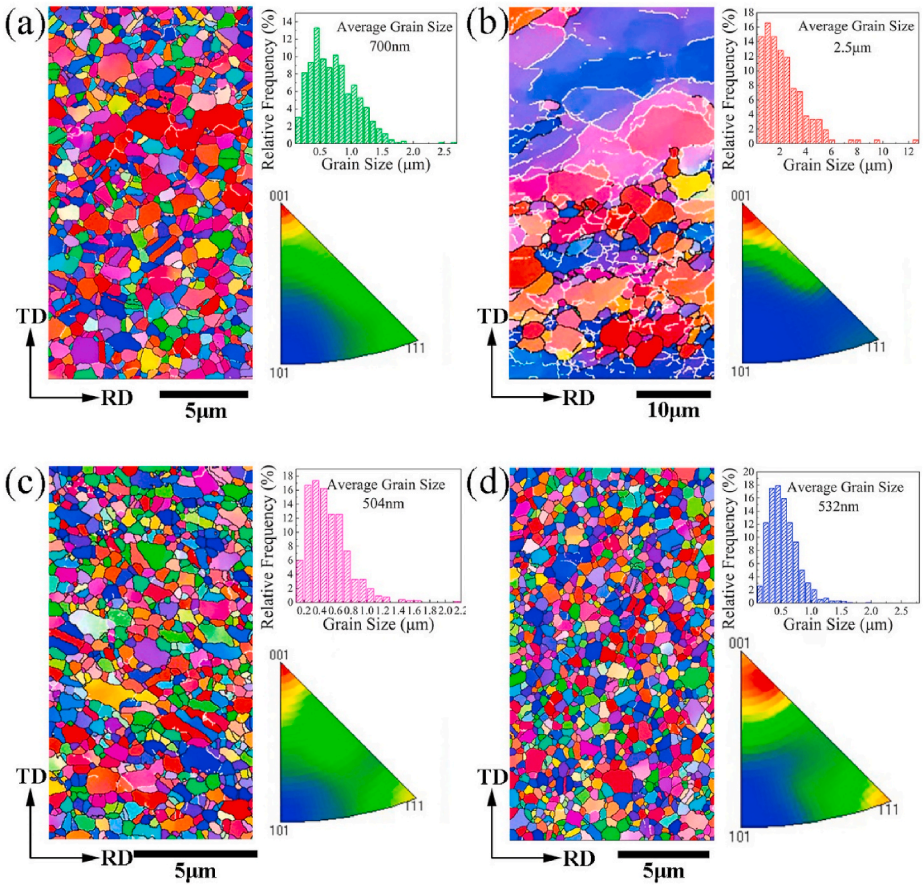

Fig. 2. EBSD IPF images and the corresponding grain size distributions, misorientation angle distributions and inverse pole figures IPF of (a) HE1000, (b) HE1100, (c) AlHE1000, (d) AlHE1000HT.

%, mean particle size < 75 μm) was also milled with Co, Cr, Fe, Ni powders to fabricate the $CoCrFeNiAl_{0.3}$ (Al: 7 at.%) HEA sample extruded at 1000 °C, named as AlHE1000. The as-extruded $CoCrFeNiAl_{0.3}$ HEA sample was solution treated at 1150 °C for 1 h, followed by water quenching and aging at 550 °C for 80 h. The heat-treated sample was named as AlHE1000HT. The sample details and fabrication process have been listed in Table 1.

The chemical compositions of the extruded CoCrFeNi and $CoCrFeNiAl_{0.3}$ samples were determined by an X-ray fluorescence spectrometer (XRF-1800, Shimadzu, Japan) and were listed in Table 2. The as-milled powders were characterized by X-ray diffraction (XRD, D8Adcance, Bruker AXS, Germany) with Cu kα radiation. The as-fabricated HEA samples were characterized by XRD, electron back scattering diffraction (EBSD, Aztec HKL Max, Oxford, UK) on scanning electron microscope (SEM, TESCAN Mira3, Czech), transmission electron microscope (TEM, JEM-2100F, JEOL, Japan) and scanning transmission electron microscope (STEM, JEM-ARM200F, JEOL, Japan). Approximately 80–150 nanoparticles in 3 different STEM images were measured by ImageJ software to determine the size and volume fraction. The EBSD samples were prepared by grounding, mechanical polishing and vibration polishing. The TEM and STEM samples were prepared by double jet electron polishing using an electrolyte of 80% methanol +20% nitric acid with a current of 100 mA at -30 °C and followed by ion milling. The tensile test specimens were cut along the longitudinal direction of the as-fabricated samples. Dog-bone shaped specimens with gauge length of 12 mm and cross section dimensions of 3.0 × 1.5 mm^2 were used for the tensile test. The tensile test was performed using a Zwick/Roell Z100 testing machine at room temperature with a strain rate of 5 × 10^{-4} s^{-1}. Three tensile specimens were tested for each HEA sample.

3. Results

Fig. 1(a) shows the XRD patterns of the milled powders with different milling time. It can be found that with increasing milling time from 0 to 84 h, the diffraction peaks of Co, Cr, Fe and Ni disappeared gradually and the strong FCC and weak BCC diffraction peaks were detected, suggesting that the CoCrFeNi solid solution was formed. The apparent broadening and left-shift of the FCC diffraction peaks were also observed with the increase of milling time, which is likely due to grain refinement and the increase of the degree of lattice strain caused by severe plastic deformation during mechanical milling. The crystalline size and lattice strain were calculated based on the XRD results using Williamson-Hall equation [24]:

$$\beta \cos\theta = \frac{0.9\lambda}{D} + \varepsilon \sin\theta \quad (1)$$

where β is the half full width of corresponding diffraction peak, θ is the angle of diffraction peak, λ is the wavelength of $Cu_{\alpha 1}$, ε is the lattice strain.

The insert figure in Fig. 1(a) showed the changes of crystalline size and lattice strain with milling time. It can be seen that the crystalline size decreased gradually from 167 (±2) nm to 74 (±1) nm, while the lattice strain increased from 0.54% (±0.01%) to 1.22% (±0.02%) with milling time increasing from 12 to 84 h. Fig. 1(b) shows the XRD patterns of the as-extruded and as-heat treated HEAs samples. It was clearly observed that a CoCrFeNi solid-solution with single phase FCC structure was formed after extrusion. In addition, it was also found that for the CoCrFeNi HEAs with increasing extrusion temperature from 1000 to 1100 °C the intensity of the major peak (1 1 1) became weaker, while the intensity of the minor peak (1 0 0) increased, indicating that increasing

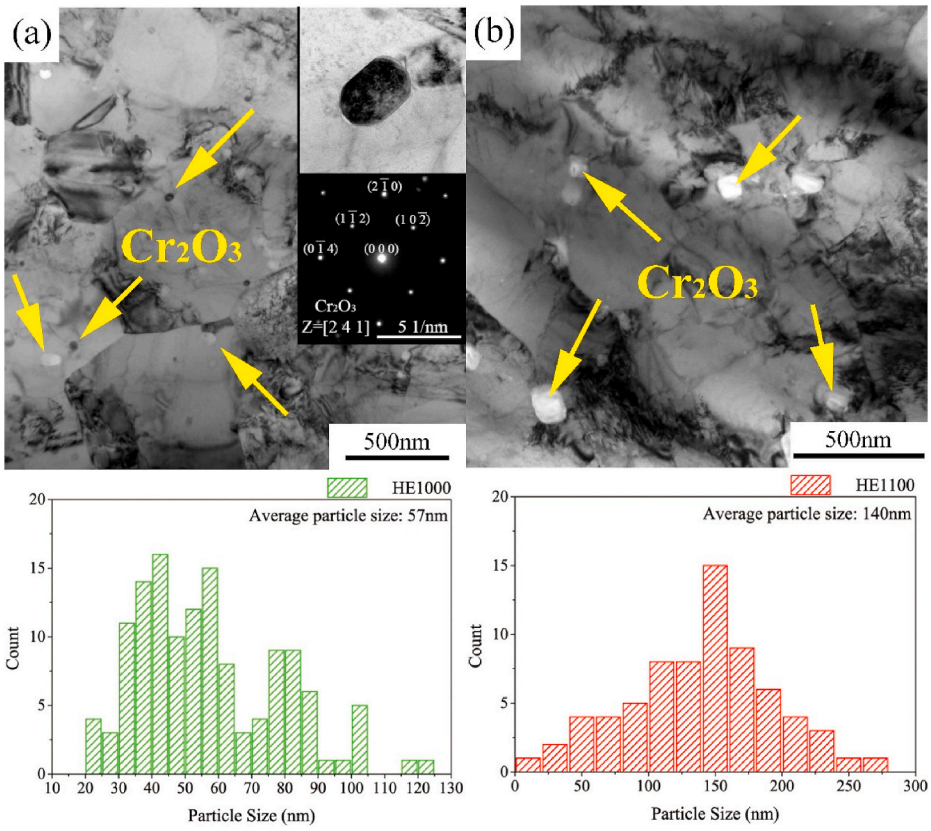

Fig. 3. TEM bright field images and the corresponding Cr_2O_3 particle size distribution of the as-fabricated CoCrFeNi HEA samples: (a) HE1000; (b) HE1100.

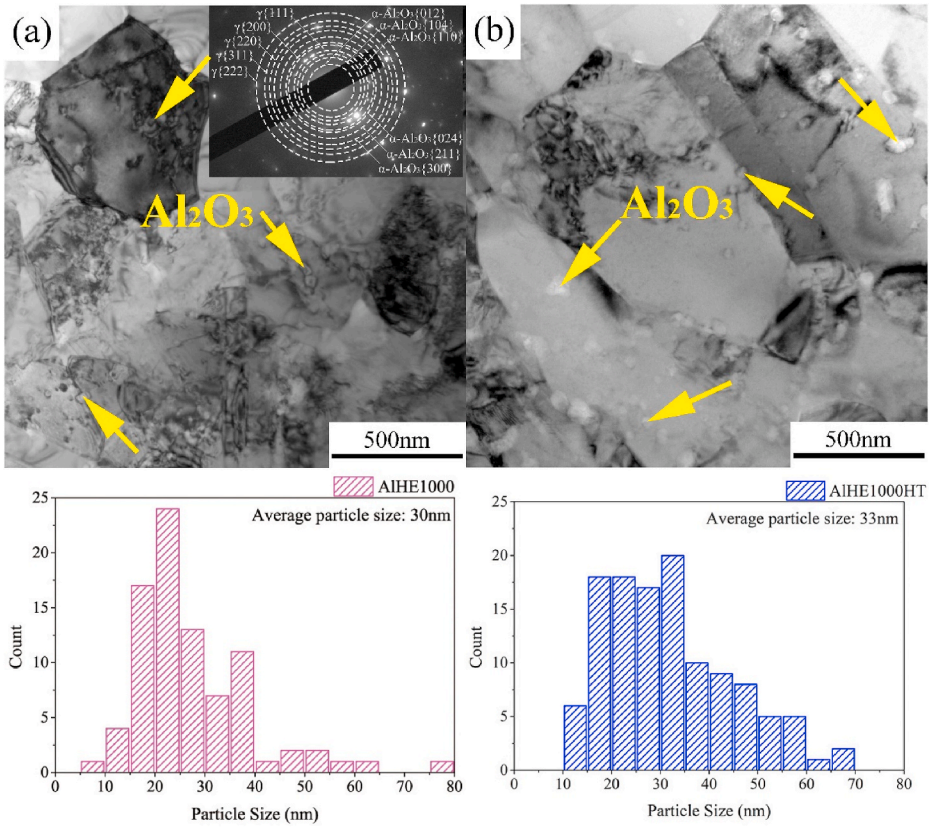

Fig. 4. TEM bright field images and Al_2O_3 particle size distribution of the as-fabricated $CoCrFeNiAl_{0.3}$ HEA samples: (a) AlHE1000; (b) AlHE1000HT.

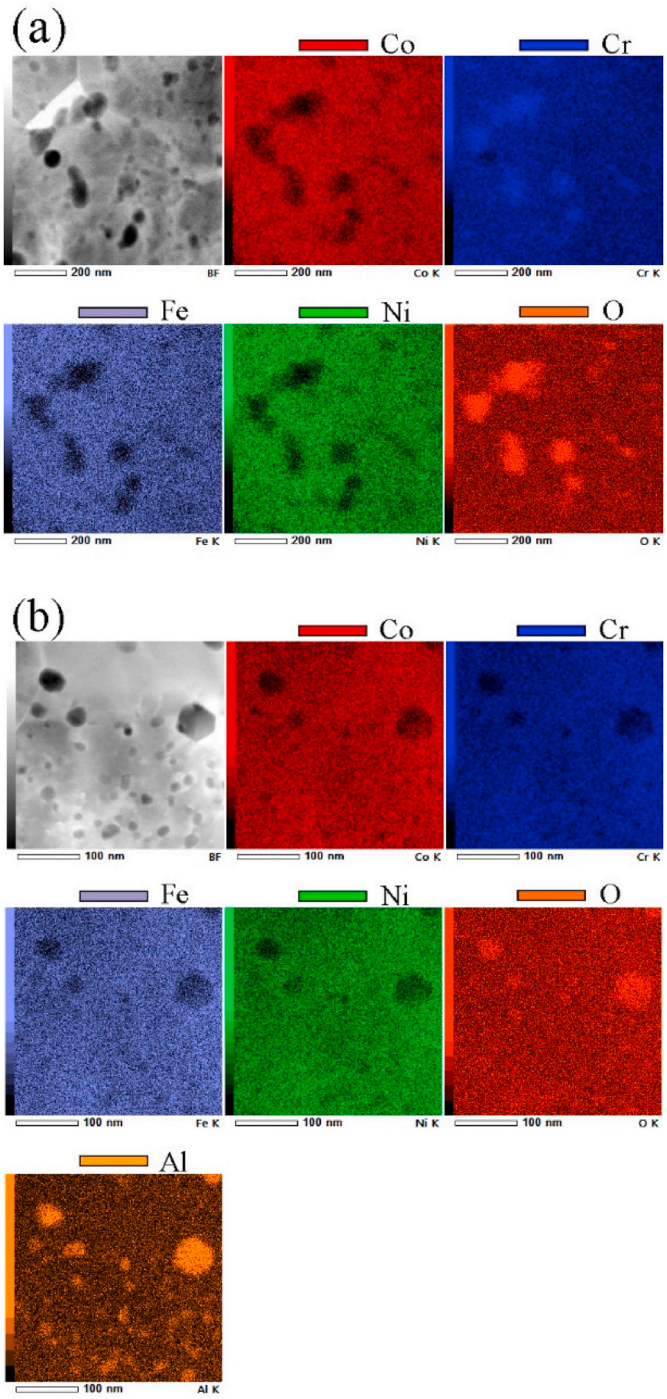

Fig. 5. STEM high angle annular dark field (HAADF) images and the corresponding EDS element mappings of the HEA samples: (a) HE1000; (b) AlHE1000.

extrusion temperature has brought about a change in microtexture.

Fig. 2 shows the EBSD images, the corresponding grain size distributions and inverse pole figures of the HEA samples. It can be observed that the HE1000 exhibited a microstructure consisting of equiaxed grains with an average size of 700 nm, as shown in Fig. 2(a). With increasing the extrusion temperature from 1000 to 1100 °C, a heterogeneous microstructure consisting of coarse grains and fine grains was formed. The corresponding grain size distribution result showed that the average grain size was 2.5 μm, as shown in Fig. 2(b). When adding Al element, the AlHE1000 sample demonstrated a finer equiaxed grain with mean size of 504 nm, as shown in Fig. 2(c). After heat treatment, the grain size increased slightly to 532 nm, indicating a good thermal stability at high temperature, as shown in Fig. 2(d).

Fig. 3(a) is the TEM bright field image of the HE1000 sample. It can be found that fine nanoparticles were observed in the CoCrFeNi HEA matrix. The high magnification TEM image indicated that the nanoparticle was nearly spherical with a diameter of about 60 nm. The corresponding selected area diffraction pattern was acquired with the electron beam paralleling to Cr_2O_3 [2 4 1] zone axis, confirming that the nanoparticle was Cr_2O_3. The particle size distribution of the Cr_2O_3 nanoparticles indicated that the mean size was 57 nm. With increasing extrusion temperature to 1100 °C, the Cr_2O_3 nanoparticles coarsened, as illustrated in Fig. 3(b), showing that the mean size of the Cr_2O_3 nanoparticles was 140 nm.

As shown in Fig. 4 (a), the TEM BF image of the AlHE1000 sample indicated that finer nanoparticles were detected both in grain interiors and on grain boundaries. The corresponding SAED pattern indicated that these nanoparticles were likely α-Al_2O_3. It is noted that no Cr_2O_3 diffraction signals were detected in the SAED pattern, illustrating that the formation of Cr_2O_3 nanoparticles were totally suppressed. Based on the average particle size distribution of α-Al_2O_3 nanoparticles, the mean particle size of the α-Al_2O_3 nanoparticles was 30 nm. After heat treatment, the Al_2O_3 nanoparticle size did not change, suggesting a good thermal stability, as displayed in Fig. 4(b).

Fig. 5 presents the STEM HAADF images and the corresponding EDS elements mapping of the HE1000 and AlHE1000 samples. It can be observed that Co, Cr, Fe and Ni elements are distributed homogeneously in the CoCrFeNi matrix, as shown in Fig. 5(a). In addition, the Cr and O rich nanoparticles were also detected in the HEA matrix, confirming that they are Cr_2O_3 particles. Similar observations were also made in AlHE1000 sample, confirming the formation of Al_2O_3 nanoparticles, as demonstrated in Fig. 5(b).

Fig. 6 shows the STEM results of the AlHE1000HT sample. As shown in Fig. 6(a) and (b), the nano-sized precipitates were observed in grain interior of the AlHE1000HT sample. These precipitates are nearly spherical with a mean diameter of about 4.5 nm. Fig. 6(c) displays the high resolution TEM image of the AlHE1000HT sample, which indicated that the precipitates were fully coherent with the matrix. This was confirmed by the corresponding SAED pattern acquired along the $[0\ 1\ 1]_{fcc}$ zone axis, exhibiting super lattice reflections at (0 1 1) and (1 0 0) positions of the $[0\ 1\ 1]_{fcc}$ diffraction pattern, as shown in Fig. 6(c). Based on the SAED result, it can be determined that the precipitates are $L1_2$ structured γ′-Ni_3Al. The corresponding inverse fast Fourier transformation (IFFT) showed that dramatic lattice distortion was observed around the precipitates.

Fig. 7 shows the tensile engineering stress-strain curves of the HE1000, HE1100, AlHE1000 and AlHE1000HT samples. The corresponding tensile properties are shown in Table 3. It can be seen that the yield strength (YS), ultimate tensile strength (UTS) and elongation to fracture (EL) of the HE1000 and HE1100 samples were 884 and 540 MPa, 1070 and 854 MPa, and 21.8% and 23.9%, respectively, suggesting that increasing extrusion temperature from 1000 to 1100 °C caused a significant strength decrease and a slight ductility increase. For the AlHE1000 samples, the YS, UTS and EL were 1231 MPa, 1283 MPa and 6.1%, suggesting that adding Al element caused an apparent strength increase and ductility decrease. It is noted that, after heat treatment, the YS, UTS and elongation to fracture increased simultaneously to 1335 MPa, 1346 MPa and 7.9%, respectively.

4. Discussion

4.1. Microstructure evolution

The HE1000 samples demonstrate a microstructure consisting of fine equiaxed grains and dispersed Cr_2O_3 nanoparticles. The equiaxed grains may result from dynamic recrystallization caused by plastic deformation during extrusion. This is confirmed by the EBSD IPF result showing the

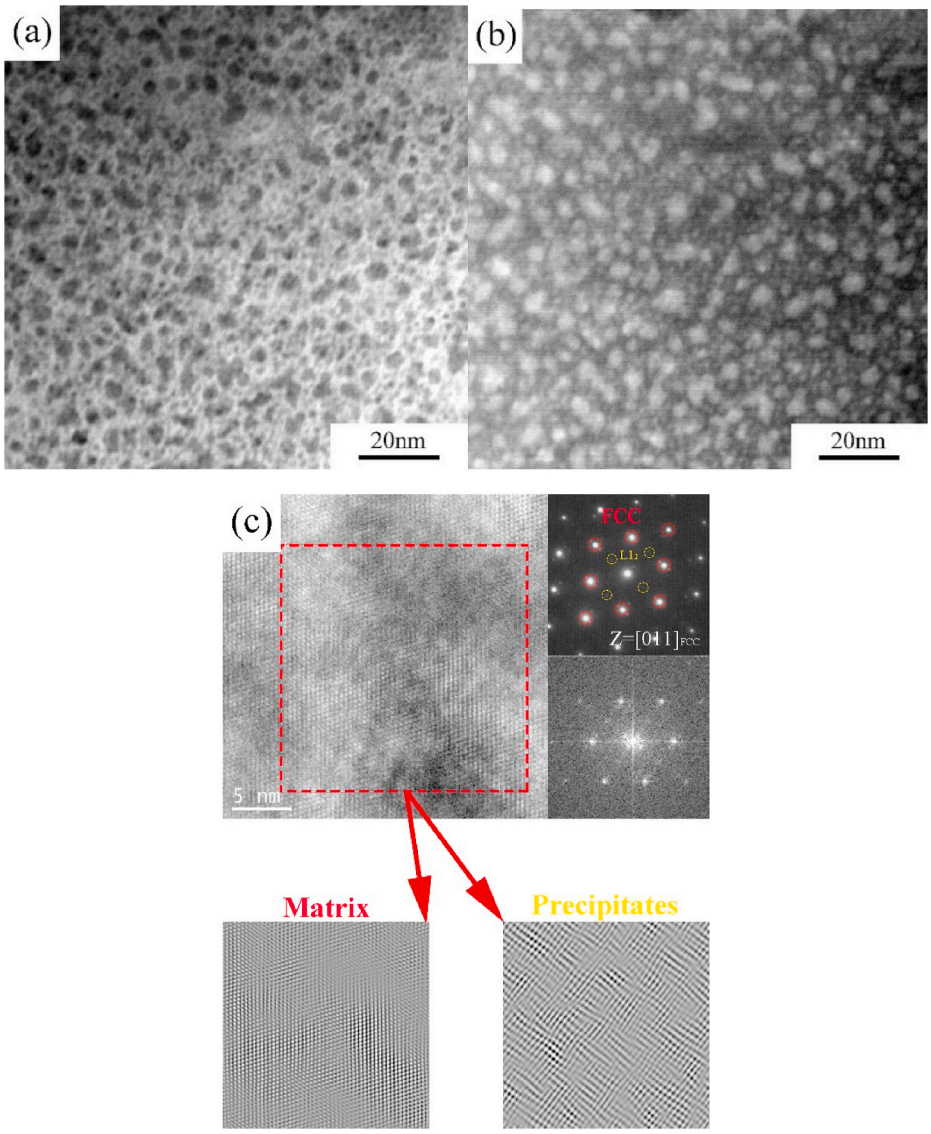

Fig. 6. (a) STEM bright field (BF), (b) HADDF and (c) high resolution TEM images of the AlHE1000HT sample.

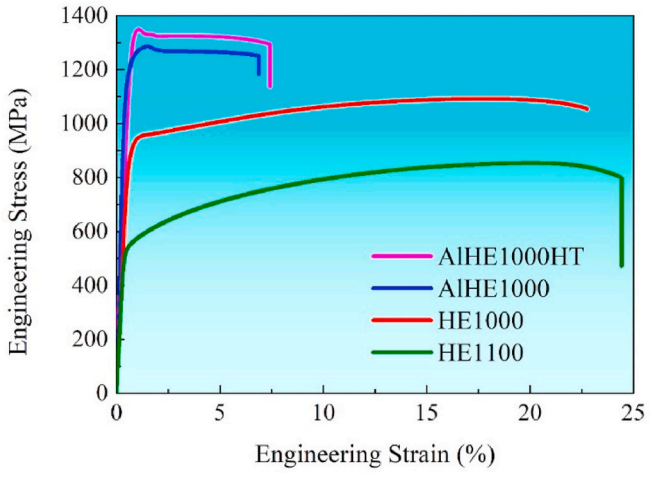

Fig. 7. Engineering tensile stress-strain curves of the HEA samples.

presence of major <001> recrystallization texture in the HE1000 sample. With increasing the extrusion temperature from 1000 to 1100 °C, the further recrystallization and non-uniform growth of the recrystallized grains occur, leading to a significant increase of grain size from 700 nm to 2.5 μm. The observation of the increased degree of recrystallization is strongly supported by the improved intensity of <001> recrystallization texture indicated by the XRD patterns (Fig. 1 (b)) and EBSD IPF image (Fig. 2(b)).

Table 3
Tensile properties of the CoCrFeNi and $CoCrFeNiAl_{0.3}$ HEA samples.

Samples	YS (MPa)	UTS (MPa)	Elongation to fracture (%)
HE1000	884 ± 14	1070 ± 16	21.8 ± 0.8
HE1100	540 ± 3	854 ± 4	23.9 ± 3.2
AlHE1000	1231 ± 39	1283 ± 13	6.1 ± 0.5
AlHE1000HT	1335 ± 9	1346 ± 2	7.9 ± 0.4

The formation of dispersed Cr_2O_3 nanoparticles in the CoCrFeNi HEA samples may associate with the reaction between Cr powders and oxygen coming from the oxide layer on the surface of the starting powders. It was reported that comparing with Co, Fe and Ni elements, Cr has the lowest Gibbs free energy of formation with oxygen (Cr_2O_3: -1355 kJ/mol, CoO: -356 kJ/mol, FeO: -400 kJ/mol, NiO: -337 kJ/mol at 1000 °C

Table 4
Parameters for the calculation of grain boundary energy of the CoCrFeNi and $CoCrFeNiAl_{0.3}$ HEA samples.

Related Parameters	Values
a_0 (nm)	0.358
N_A	6.02×10^{23}
R (J/mol K)	8.314
Q_v (kJ/mol) [31]	258
Q_{gb} (kJ/mol) [31]	158

[25]) and the most rapid diffusion rate (Cr: 1.69×10^{-13} m^2/s, Co: 0.98×10^{-13} m^2/s, Fe: 1.30×10^{-13} m^2/s, Ni: 0.95×10^{-13} m^2/s in CoCrFeMnNi [26]). Hence, it can be envisaged that the reaction between Cr and O occurred quickly during heating and extrusion. With increasing extrusion temperature from 1000 to 1100 °C, the size of Cr_2O_3 nanoparticle increases from 57 to 140 nm. This is probably owing to the Ostwald ripening caused by increased extrusion temperature. When adding Al into CoCrFeNi HEA, instead of Cr_2O_3 particles the Al_2O_3 nanoparticles formed due to two reasons: (1) the lower Gibbs free energy of formation of Al_2O_3 than that of Cr_2O_3 (Al_2O_3: -1837 kJ/mol, Cr_2O_3:-1355 kJ/mol at 1000 °C [25]); (2) the lower diffusivity of Al than that of Cr in high entropy alloy (D_{Al}: -14.00 m^2/s > D_{Cr}: -15.34 m^2/s [27]).

It is well recognized that grain size is closely related to the migration of grain boundaries which decreases grain boundary energy by providing driving force for grain growth. Buker et al. deduced the following equation to estimate driving force for grain growth [12,13],

$$P_{gb} = \frac{2\alpha\gamma_{gb}}{D_g} \tag{2}$$

where α is the geometric constant, γ_{gb} is the grain boundary energy and D_g is the diameter of grain size. The grain boundary energy γ_{gb} is the temperature dependence which was given by Gupta et al. [28], Borisov et al. [29] and Vaidya [30]:

$$\gamma_{gb} = \frac{RT}{2a_0{}^2N_A} ln\left(\frac{D_{0_{gb}}}{D_{0_v}}\right) + \frac{1}{2a_0{}^2N_A}\left(Q_v - Q_{gb}\right) \tag{3}$$

where a_0 is the lattice parameter, N_A is the Avogadro's number, R is gas constant, T is the temperature, Q_v is the bulk diffusion parameter and Q_{gb} is the grain boundary diffusion parameter. All values of above parameters are listed in Table 4. Based on above, the γ_{gb} is given as,

$$\gamma_{gb} = 0.62 + \left(1.52 * 10^{-4}\right) * T \tag{4}$$

Furthermore, the second phase particles can exert pinning effects, known as Zener pinning [14], on grain boundaries to restrict grain growth by competing with the driving force for grain growth. The Zener pinning pressure is relating to diameter and volume fraction of particles, which is given as,

$$P_Z = \frac{3F_v\gamma_{gb}}{D_p} \tag{5}$$

where γ_{gb} is the grain boundary energy, F_v and D_p are the volume fraction and diameter of particles, respectively.

Therefore, the driving force for grain growth, when considering the Zener pinning effects, can be estimated by the equation as,

$$\Delta P = P_{gb} - P_z \tag{6}$$

Based on the equation above, the calculated ΔP for HE1000 and AlHE1000 are 3.05 MPa and 1.98 MPa, which can explain the reason for the apparent reduction of grain size when adding Al element into the CoCrFeNi HEA, as shown in Fig. 2 (a) and (c).

It was reported [21,31] that fine spherical continuous precipitates and coarse discontinuous precipitates form respectively in grain interiors and at grain boundaries of the CoCrFeNi-based HEAs fabricated by casting and heat treatment. The spherical intragranular precipitates are coherent [20–23] with the HEAs matrix to reduce the barrier for homogeneous nucleation [32,33] and decrease the free energy of precipitate/matrix interface [34]. The large lamellar-like discontinuous precipitates may result from heterogenous nucleation associating with the segregation of Al or Ti solute atoms near grain boundaries [21,35], which could reduce the grain boundary energy. It is believed that grain boundaries can act as heterogenous sites for discontinuous precipitation, and atom diffusion along grain boundary is faster than that in matrix lattice [31]. This could facilitate the formation of coarse discontinuous precipitates at grain boundaries. It is interesting to note that in this study the discontinuous precipitates are not observed at grain boundaries. This is likely due to the homogeneous dissolution of Al solute atoms in HEA matrix caused by high energy ball milling, which inhibits the occurrence of Al atoms segregation on grain boundaries. Hence the precipitates can nucleate homogeneously in grain interiors. Moreover, the growth of discontinuous precipitates usually accompanied with grain boundary migration [35], whilst in this study the boundary migration is inhibited by the dispersed Al_2O_3 nanoparticles at grain boundaries, which eliminates the occurrence of discontinuous precipitation.

4.2. Mechanical properties

Comparing with the HE1100 sample, the HE1000 exhibit a significant strength increase with a slightly lower ductility, as reflected by the increase of YS and UTS from 540 and 854 MPa to 884 and 1070 MPa, and the decrease of EL from 23.9% to 21.8%, respectively. This finding shows that the decrease of ductility caused by grain refinement (from 2.5 μm to 700 nm) could be compensated by reducing nanoparticle size (from 140 nm to 57 nm). It was reported [11] that when the grain size was reduced to the ultrafine/nano scale, the dislocation source shifted from grain interiors to grain boundaries gradually. This could cause the lack of movable dislocations in grain interior and weaken the work hardening ability of materials, reducing the ductility of the materials. Interestingly, the finer nanoparticles (with mean size of 57 nm) in the HE1000 sample could accumulate dislocation by pinning effect, which is contributed to the improvement of the work hardening ability, sustaining the ductility of the materials [22,36,37].

When adding Al in the HEA samples, it demonstrates further strength increase and ductility reduction, with the YS and UTS being increased from 884 and 1070 MPa to 1231 and 1283 MPa respectively and the EL largely reduced from 21.8% to 6.1% (HE1000 vs. AlHE1000). This significantly decrease in ductility indicates that the loss of work hardening ability caused by the further reduction of grain size from 700 to 504 nm could not be compensated by the pinning effect of fine nanoparticles on dislocations. It is reported that the "Frank-Read" dislocation sources in grain interiors are very limited or even disappeared with the decrease of grain size, and they finally transit from grain interiors to grain boundaries [11]. Grain boundaries can act as the dislocation sources and sinks where the emission and absorption of dislocations are in very high rate, and the movable dislocations cannot accumulate. The lack of movable dislocations in grain interior destroys the work hardening ability, and eventually reflects with a short uniform deformation and poor ductility of the materials. The significant decline of work hardening ability with decreasing grain size was reported in ultrafine grained 1100-Al and IF steel [38], which has a well agreement with our observation. Other similar results have also been reported by Xu et al. [39], Sun et al. [40] and Yoshida et al. [41]. Furthermore, the Al_2O_3 nanoparticles demonstrate smaller particle size and higher volume fraction than those of the Cr_2O_3 nanoparticles, which could facilitate the dislocation accumulation by the pinning effect. It can be envisaged that the smaller grain size and finer oxide particles led to the work hardening rate lower than the flow stress which is nearly close to the ultimate stress the materials can sustain, leading to necking occurs immediately after yielding. It is noted that the work hardening ability is retained after heat

Table 5
Parameters for the calculation of strengthening mechanisms of the CoCrFeNi and $CoCrFeNiAl_{0.3}$ HEA samples.

Parameters	Alloys			
	HE1100	HE1000	AlHE1000	AlHE1000HT
M [16]	3.06	3.06	3.06	3.06
G (GPa)	80	80	80	80
a (nm)	0.357	0.357	0.358	0.358
c (at.%)	0	0	7	0
α [16]	0.16	0.16	0.16	0.16
b	0.252437	0.253568	0.253929	0.253074
$\rho(m^{-2})$	2.35×10^{12}	1.7×10^{13}	2.7×10^{13}	1.8×10^{12}
ε (%)	0.043	0.079	0.1	0.007
Dg (nm)	2500	700	504	532
K_{HP} ($MPa\sqrt{m}$) [7]	0.494	0.494	0.494	0.494
D_p (nm)	140	57	30	33
f (%)	2.59	2.12	2.58	2.58
V [16]	0.26	0.26	0.26	0.26

treatment, as confirmed by the simultaneously increase of strength and ductility (YS: 1231 MPa–1335 MPa, EL: 6.1%–7.9%). This may associate with the presence of coherent γ′-Ni_3Al nanoprecipitates and the decrease of dislocation density, which are contributed to the dislocation storage in grain interior.

In this study, the improved strength may be attributed to the contributions from several strengthening mechanisms: grain boundary strengthening, nanoparticle strengthening, precipitate strengthening, solid solution strengthening, dislocation strengthening [42]. The yield strength σ_y can be quantitatively analyzed by arithmetic model which simply calculating the sum of these four strengthening contributions,

$$\sigma_y = \sigma_0 + \sigma_{ss} + \sigma_{dis} + \sigma_g + \sigma_{or} + \sigma_p \tag{7}$$

The σ_0, σ_{ss}, σ_{dis}, σ_g, σ_{or}, σ_p are strengthening contributions of lattice friction, solid solution, dislocation, grain boundary, nanoparticles and precipitates, respectively.

For high entropy alloys, the definition of solvent and solution is not clear since they are the equiatomic and concentrated solid solution. Hence the traditional solid solution strengthening model cannot be used in such a complicated solid-solution system. Recently, a simple way to define solvent and solution in $(FeCoNiCr)_{94}Ti_2Al_4$ and $Al_{0.1}CoCrFeNi$ high entropy alloy (i.e. Ti and Al as the solute atoms and CoCrFeNi as the solution matrix) have been reported [20,39]. In this study, we similarly treat the CoCrFeNi as the solution matrix and Al as the solute atom so that the solid solution strengthening can be described based on the traditional theory [20,39,43]:

$$\Delta\sigma_{ss} = \left(MG\varepsilon_s^{3/2}c^{1/2}\right) / 700 \tag{8}$$

$$\varepsilon_s \approx \left|\frac{\varepsilon_G}{1+0.5|\varepsilon_G|} - 3\varepsilon_a\right| \tag{9}$$

$$\varepsilon_a = \frac{1}{a}\frac{\partial a}{\partial c} \tag{10}$$

$$\varepsilon_G = \frac{1}{G}\frac{\partial G}{\partial c} \tag{11}$$

where M is the Taylor factor, G is the shear modulus, c is the atomic ratio of Al in the matrix (7 at.% for the $CoCrFeNiAl_{0.3}$), ε_a is the fraction change in lattice parameter per unit concentration of solute atom, ε_G is the fraction change in shear modulus. ε_G is usually ignored in calculation. All the values of related parameters are provided in Table 5. According to XRD results, three peaks of each sample are measured to determine the lattice parameters based on Bragg's law, which are 0.357 nm, 0.357 nm, 0.358 nm and 0.358 nm respectively for the HE1100, HE1000, AlHE1000 and AlHE1000HT samples. It can be found that the addition of Al does not change the lattice parameter too much. This is likely due to that the content of Al is only 7 at.% and most of the Al atoms were consumed by reacting with O and Ni elements to form Al_2O_3 and Ni_3Al. Therefore, the strengthening contribution from solid-solution of Al into the matrix is estimated to be 4 MPa in AlHE1000, as shown in Table 6. For the AlHE1000HT sample, we assume that all the Al solute atoms have been precipitated out after heat treatment, so the solid solution strengthening of Al solute atoms is ignored.

It is believed that a number of dislocations are produced during hot extrusion of the CoCrFeNi HEA samples, which are contributed to the dislocation strengthening by interacting with each other during plastic deformation. The dislocation strengthening can be estimated by Balley-Hirsch formula which is given as [42]:

$$\Delta\sigma = M\alpha Gb\rho^{1/2} \tag{12}$$

where M is the Taylor factor, α is the strength coefficient of the dislocation network, G is the shear modulus, b is the Burgers vector, and ρ is the dislocation density, which can be estimated through the Williamson-Hall method [24,44],

$$\rho = \frac{2\sqrt{3}\varepsilon}{D_g b} \tag{13}$$

$$\beta\cos\theta = \frac{K\lambda}{D_g} + (4\sin\theta)\varepsilon \tag{14}$$

where ε is the microstrain, D_g is the grain size, K is a constant ~0.9, β is the full width at half maximum of a diffraction peak, λ is the wavelength of Cu Kα radiation taken as 0.15405 nm, and θ is the Bragg angle of the certain peak. The estimated dislocation strengthening contributions of HE1100, HE1000, AlHE1000 and AlHE1000HT are 15 MPa, 41 MPa, 51 MPa and 13 MPa, respectively, as summarized in Table 6.

To evaluate the contribution of grain boundaries strengthening to the increment of strength, the Hall-Petch relationship is used, which is given as [45,46]:

$$\Delta\sigma_g = \frac{K_{HP}}{\sqrt{D_g}} \tag{15}$$

where K_{HP} is the Hall-Petch coefficient, D_g is the grain size. The calculated strengthening contributions of grain boundaries for the HE1100, HE1000, AlHE1000 and AlHE1000HT samples are 312 MPa, 590 MPa, 696 MPa and 677 MPa, respectively, as summarized in Table 6.

As to the estimation of nanoparticle strengthening, the Orowan mechanism and shearing mechanism can be used. Owing to the incoherence relationship between the Cr_2O_3/Al_2O_3 nanoparticles and HEA matrix, it can be determined that the Orowan mechanism dominates the strengthening of Cr_2O_3/Al_2O_3 nanoparticles. For the coherent γ′-Ni_3Al precipitates, the strength contribution is governed by either the shearing

Table 6
Contributions of various strengthening mechanisms to yield stress of the CoCrFeNi and $CoCrFeNiAl_{0.3}$ HEA samples (Unit:MPa).

Samples	σ_0	σ_{ss}	σ_g	σ_{dis}	σ_{or}	σ_p	$YS_{arithmetic}$	$YS_{quadratic}$	$YS_{experimental}$
HE1000	125	0	590	41	202	0	958	890	884
HE1100	125	0	312	15	109	0	561	521	540
AlHE1000	125	4	696	51	489	0	1365	1261	1231
AlHE1000HT	125	0	677	13	452	220	1490	1427	1335

or Orowan mechanisms, depending on which holds a smaller strength increment [42]. For Orowan mechanism, the strengthening contribution can be estimated by the following equation [47]:

$$\Delta\sigma_{or} = M\frac{0.4Gb}{\pi\lambda}\frac{ln\left(\sqrt{\frac{2}{3}}\frac{D_p}{b}\right)}{\sqrt{1-\nu}} \tag{16}$$

$$\lambda = \sqrt{\frac{2}{3}}D_p\left(\sqrt{\frac{\pi}{4f}}-1\right) \tag{17}$$

where λ is the particle distance, D_p is the particle diameter, $\nu = 0.26$ is the Possion's ration, f is the volume fraction of intragranular particles. Here the presence of γ'-Ni_3Al precipitates between adjacent Al_2O_3 particles is not taken into account for the interparticle distance, as the analysis in next paragraphs showed that dislocation shearing is likely the operative mechanism for the γ'-Ni_3Al precipitates. The relative data of every terms in the equations are listed in Table 5. The strengthening contributions of the Cr_2O_3/Al_2O_3 nanoparticles are 109 MPa, 202 MPa, 489 MPa and 452 MPa, respectively, for the HE1100, HE1000, AlHE1000 and AlHE1000HT samples, as shown in Table 6.

To calculate the strengthening contribution of the γ'-Ni_3Al precipitates, firstly we assume that dislocation shearing mechanism is operative due to the coherent relationship between the precipitate and matrix. Three contribution factors including ordering strengthening $\Delta\sigma_O$ (occurs during shearing), coherency strengthening $\Delta\sigma_C$ and modulus strengthening $\Delta\sigma_M$ (make contributions before shearing) should be considered [20,21], the equations for these two factors have been summarized as [20,48,49]:

$$\Delta\sigma_O = M\cdot 0.81\frac{\gamma_{APB}}{2b}\left(\frac{3\pi f}{8}\right)^{1/2} \tag{18}$$

$$\Delta\sigma_C = M\alpha_\varepsilon(G\varepsilon)^{3/2}\left(\frac{Df}{Gb}\right)^{1/2} \tag{19}$$

$$\Delta\sigma_M = M0.0055(\Delta G)^{3/2}\left(\frac{2f}{G}\right)^{1/2}\left(\frac{D}{2b}\right)^{3m/2-1} \tag{20}$$

where M is the Taylor factor, γ_{APB} is the antiphase boundary (APB) energy (0.12 J/m^2 for the Ni_3Al precipitates in Ni-based superalloy [20]), b is the Burger vector, $f = 12\%$ is the volume fraction of γ'-Ni_3Al precipitates (calculated using the mass of residual Al after oxidation and suppose that all the residual Al atoms reacted with Ni to form Ni_3Al), $\alpha_\varepsilon = 2.6$ is a constant for FCC structure, G is the shear modulus, ε is the constrained lattice parameter mismatch, $\varepsilon \approx 2/3(\Delta a/a)$ ($\Delta\alpha$ is the difference of lattice constant between γ'-Ni_3Al and FCC matrix calculated by XRD results [20], D is the mean diameter of precipitates, ΔG is the shear modulus mismatch between the precipitates and the matrix, $m = 0.85$ is a constant [48]. The calculated values of $\Delta\sigma_O$ $\Delta\sigma_C$ and $\Delta\sigma_M$ are 220, 31 and 11 MPa, respectively. Since the $\Delta\sigma_O > \Delta\sigma_C + \Delta\sigma_M$, the ordering strengthening during shearing dominated the contribution [20,21]. The experimental strength increment contributed by precipitation hardening was 202 MPa (dislocation annihilation and change of grain/Al_2O_3 size during heat treatment have been considered), which is closed to the calculation result. The overestimated value is possibly due to the unknown γ_{APB} of Ni_3Al in high entropy alloys. In Orowan mechanism, the calculated value of strength increment is 4289 MPa based on equations (16) and (17), which demonstrated a significant deviation from our experiment result (YS: 1335 MPa), implying that dislocation shearing is likely the operative mechanism for the γ'-Ni_3Al precipitates. Several studies on γ'-type precipitation hardening CoCrFeNi based HEAs have been reported in literatures, which exhibited excellent YS and UTS after T6 treatment, for instance, 490 MPa and 850 MPa in $Al_{0.3}$CoCrFeNi HEA [50], 1005 MPa and 1273 MPa in $(FeCoNiCr)_{94}Ti_2Al_4$ HEA [20], and 863.5 MPa and 1285.9 MPa in $Al_{0.3}$FeCoCrNi HEA [51]. This illustrates that the result of 1335 MPa and 1346 MPa in this work is competitive with the other studies in the literature.

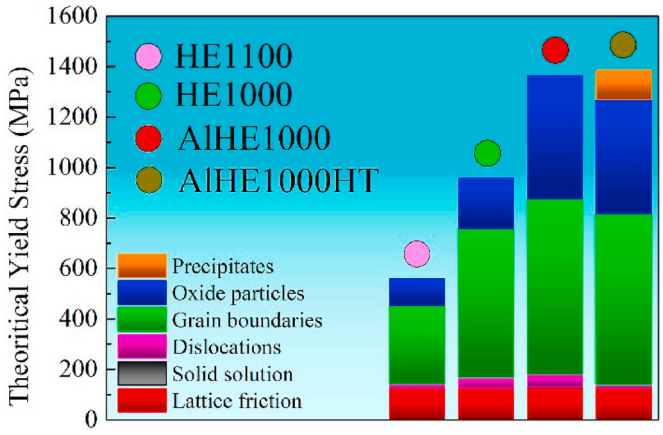

Fig. 8. Various strengthening contributions to yield stress of the HEA samples.

For clarity, a column chart is produced to show the individual strengthening contribution directly, as shown in Fig. 8. It is apparently that grain boundary strengthening and Orowan strengthening dominant the strengthening mechanisms of the materials. In addition, it can also be seen that the calculated yield stress values of all samples based on the arithmetic model are bigger than the experimental results, as shown in Table 6. This may associate with the interaction between grain boundaries and intergranular nanoparticles. It is reported [16] that the number of intergranular nanoparticles is large in ultrafine grained nanocomposites due to the improved grain boundary density. This could increase the particle-matrix interface and reduce the number of dislocations emitted from grain boundaries where the dislocation sources are formed, which should be taken into account to affect the Hall-Petch coefficient and grain boundaries strengthening. Except for that, we just added up various strengthening iterms based on the arithmetic model, while the superposition relationship among them was not considered (e.g. dislocation strengthening and grain boundary strengthening). It is believed that traditional dislocation pile-up theory is not applicable in ultrafine/nano-grained materials as the dislocations possibly emit from the grain boundaries. Therefore, the grain boundary dislocation theory based on Taylor relationship could be employed. Due to the existence of high density of grain boundaries in ultrafine/nano-grained materials, the number fraction of the intergranular nanoparticles increases. This could increase particle-matrix interface and reduce the number of dislocations emitted from grain boundaries, which consequently affect the Hall-Petch coefficient and grain boundary strengthening. In the light of these considerations, a new strengthening model has been established based on the quadratic mode [16,52], and the superposition between dislocation and grain boundary strengthening as well as the modified Hall-Petch coefficient can be estimated by the model, which is expressed as:

$$\sigma_y' = \sigma_0 + \sqrt{\Delta\sigma_d{}^2 + \Delta\sigma_g'{}^2} + \Delta\sigma_{or}' + \Delta\sigma_p \tag{21}$$

$$\Delta\sigma_g' = \alpha MGb\sqrt{3m\left(1-\frac{f_{inter}D_g}{2D_{inter}}\right) + m_{pie}\frac{6f_{inter}D_g}{D_{inter}}}D_g{}^{-1/2} = K_{HP}{}'D_g{}^{-1/2} \tag{22}$$

$$\Delta\sigma_{or}' = \frac{M\frac{0.4Gb}{\pi}\frac{ln\left(\sqrt{\frac{2}{3}}D_{intra}\Big/b\right)}{\sqrt{1-\nu}}}{\sqrt{\frac{2}{3}}D_{intra}\left(\sqrt{\frac{\pi}{4f_{intra}}}-1\right)} \tag{23}$$

where f_{inter} and f_{intra} are the volume fraction of intergranular and

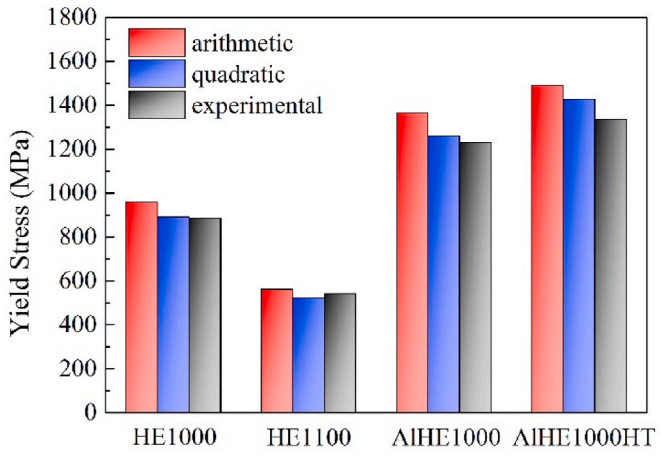

Fig. 9. Histogram of comparisons of arithmetic & quadratic model with experimental values.

intragranular particles, D_{inter} and D_{intra} are the diameter of intergranular and intragranular particles. Based on this model, the strengthening contributions are recalculated in this work (Table 6 and Fig. 9), indicating that the estimated results are in well agreement with the experimental results.

5. Conclusions

In this study, CoCrFeNi and $CoCrFeNiAl_{0.3}$ high entropy alloys were fabricated via thermomechanical consolidation of mechanical-alloyed powders. The microstructural evolution and mechanical properties were investigated, and the following conclusions were drawn:

(1) The as-extruded CoCrFeNi HEAs showed a microstructure consisting of fine equiaxed grains and dispersed Cr_2O_3 nanoparticles. With increasing the extrusion temperature from 1000 to 1100 °C, the further recrystallization and growth of the recrystallized grains occurred, leading to a significantly increase of grain size from 700 nm to 2.5 μm.

(2) Introducing Al elements into the HEA matrix not only changed the constitute of oxide particles from Cr_2O_3 to Al_2O_3 but also refined the particles from 57 nm to 30 nm. The finer Al_2O_3 nanoparticles brought about more Zener pinning force to inhibit grain boundary migration, leading to reduction of grain size from 700 to 504 nm.

(3) After heat treatment, the YS, UTS and EL increased from 1231 to 1335 MPa, 1283–1346 MPa and 6.1–7.9%, respectively. This simultaneously increase of strength and ductility may associate with the reduction of dislocation density and formation of coherent γ′-Ni_3Al nanoprecipitates in grain interiors.

(4) Based on the calculation of various strengthening mechanisms, it can be found that grain boundary strengthening and Orowan strengthening are mostly contributed to the increase of yield strength.

Data availability

The raw/processed data required to reproduce these findings cannot be shared at this time due to legal or ethical reasons.

CRediT authorship contribution statement

Z. Zhang: Writing – original draft, Investigation. **Y.H. Xie:** Methodology, Resources. **X.Y. Huo:** Formal analysis, Software. **S.L.I. Chan:** Resources. **J.M. Liang:** Supervision. **Y.F. Luo:** Data curation. **D.K.Q. Mu:** Software. **J. Ju:** Methodology. **J. Sun:** Formal analysis. **J. Wang:** Project administration.

Declaration of competing interest

The authors declare that they have no known competing financial interests or personal relationships that could have appeared to influence the work reported in this paper.

Acknowledgements

This work was supported by the National Natural Science Foundation of China (No.51971143), SJTU Global Strategic Partnership Fund (2019 SJTU-UNSW) as well as National Science and Technology Major Project (2017-VI-0013-0085).

References

[1] J.W. Yeh, S.K. Chen, S.J. Lin, J.Y. Gan, T.S. Chin, T.T. Shun, C.H. Tsau, S.Y. Chang, Nanostructured high-entropy alloys with multiple principal elements: novel alloy design concepts and outcomes, Adv. Eng. Mater. 6 (5) (2004) 299–303.
[2] M.C. Gao, J.-W. Yeh, P.K. Liaw, Y. Zhang, High-Entropy Alloys, 2016.
[3] D.B. Miracle, O.N. Senkov, A critical review of high entropy alloys and related concepts, Acta Mater. 122 (2017) 448–511.
[4] L.S. Zhang, G.L. Ma, L.C. Fu, J.Y. Tian, Recent progress in high-entropy alloys, Adv. Mater. Res. 631–632 (2013) 227–232.
[5] B. Gludovatz, A. Hohenwarter, D. Catoor, E.H. Chang, E.P. George, R.O. Ritchie, A fracture-resistant high-entropy alloy for cryogenic applications, Science 345 (6201) (2014) 1153–1158.
[6] S.J. Sun, Y.Z. Tian, X.H. An, H.R. Lin, J.W. Wang, Z.F. Zhang, Ultrahigh cryogenic strength and exceptional ductility in ultrafine-grained CoCrFeMnNi high-entropy alloy with fully recrystallized structure, Mater. Today Nano 4 (2018) 46–53.
[7] Y.H. Xie, D.S. Zhou, Y.F. Luo, T. Xia, W. Zeng, C.G. Li, J. Wang, J.M. Liang, D. L. Zhang, Fabrication of CoCrFeNiMn high entropy alloy matrix composites by thermomechanical consolidation of a mechanically milled powder, Mater. Char. 148 (2019) 307–316.
[8] H. Shahmir, T. Mousavi, J.Y. He, Z.P. Lu, M. Kawasaki, T.G. Langdon, Microstructure and properties of a CoCrFeNiMn high-entropy alloy processed by equal-channel angular pressing, Mater. Sci. Eng. Struct. Mater. Properties Microstruct. Process. 705 (2017) 411–419.
[9] B. Schuh, F. Mendez-Martin, B. Volker, E.P. George, H. Clemens, R. Pippan, A. Hohenwarter, Mechanical properties, microstructure and thermal stability of a nanocrystalline CoCrFeMnNi high-entropy alloy after severe plastic deformation, Acta Mater. 96 (2015) 258–268.
[10] A. Considère, Mémoire sur l'emploi du fer et de l'acier dans les constructions. Ann. des ponts chaussées, Mémoires Doc. relatifs à l'art des Constr, au Serv. l'ingénieur 1 (1885) 575–777.
[11] I.A. Ovid'ko, R.Z. Valiev, Y.T. Zhu, Review on superior strength and enhanced ductility of metallic nanomaterials, Prog. Mater. Sci. 94 (2018) 462–540.
[12] F.J. Humphreys, M. Hatherly, Recrystallization and Related Annealing Phenomena, Elsevier, 2012.
[13] J.E. Burke, D. Turnbull, Recrystallization and grain growth, Prog. Met. Phys. 3 (1952) 220–292.
[14] C.S. Smith, Grains, phases, and interfaces: an introduction of microstructure, Trans. Metall. Soc. AIME 175 (1948) 15.
[15] S. Praveen, J. Basu, S. Kashyap, R.S. Kottada, Exceptional resistance to grain growth in nanocrystalline CoCrFeNi high entropy alloy at high homologous temperatures, J. Alloys Compd. 662 (2016) 361–367.
[16] Y.H. Xie, Y.F. Luo, T. Xia, W. Zeng, J. Wang, J.M. Liang, D.S. Zhou, D.L. Zhang, Grain growth and strengthening mechanisms of ultrafine-grained CoCrFeNiMn high entropy alloy matrix nanocomposites fabricated by powder metallurgy, J. Alloys Compd. 819 (2020), 152937.
[17] W.H. Liu, J.Y. He, H.L. Huang, H. Wang, Z.P. Lu, C.T. Liu, Effects of Nb additions on the microstructure and mechanical property of CoCrFeNi high-entropy alloys, Intermetallics 60 (2015) 1–8.
[18] B. Gwalani, S. Gorsse, D. Choudhuri, Y.F. Zheng, R.S. Mishra, R. Banerjee, Tensile yield strength of a single bulk Al0.3CoCrFeNi high entropy alloy can be tuned from 160 MPa to 1800 MPa, Scripta Mater. 162 (2019) 18–23.
[19] R.C. Reed, The Superalloys, Cambridge University Press, Cambridge, 2006.
[20] J.Y. He, H. Wang, H.L. Huang, X.D. Xu, M.W. Chen, Y. Wu, X.J. Liu, T.G. Nieh, K. An, Z.P. Lu, A precipitation-hardened high-entropy alloy with outstanding tensile properties, Acta Mater. 102 (2016) 187–196.
[21] Y.L. Zhao, T. Yang, Y. Tong, J. Wang, J.H. Luan, Z.B. Jiao, D. Chen, Y. Yang, A. Hu, C.T. Liu, J.J. Kai, Heterogeneous precipitation behavior and stacking-fault-mediated deformation in a CoCrNi-based medium-entropy alloy, Acta Mater. 138 (2017) 72–82.
[22] T. Yang, Y.L. Zhao, Y. Tong, Z.B. Jiao, J. Wei, J.X. Cai, X.D. Han, D. Chen, A. Hu, J. J. Kai, K. Lu, Y. Liu, C.T. Liu, Multicomponent intermetallic nanoparticles and superb mechanical behaviors of complex alloys, Science 362 (6417) (2018) 933–937.

[23] Y.J. Liang, L. Wang, Y. Wen, B. Cheng, Q. Wu, T. Cao, Q. Xiao, Y. Xue, G. Sha, Y. Wang, Y. Ren, X. Li, L. Wang, F. Wang, H. Cai, High-content ductile coherent nanoprecipitates achieve ultrastrong high-entropy alloys, Nat. Commun. 9 (1) (2018) 4063.
[24] G.K. Williamson, W.H. Hall, X-ray line broadening from filed aluminium and wolfram, Acta Metall. 1 (1) (1953) 22–31.
[25] I. Barin, Thermodynamic Data of Pure Substances, American Chemical Society and American Institute of Physics fro National Bureau of Standards, 1995.
[26] K.Y. Tsai, M.H. Tsai, J.W. Yeh, Sluggish diffusion in Co–Cr–Fe–Mn–Ni high-entropy alloys, Acta Mater. 61 (13) (2013) 4887–4897.
[27] J. Dąbrowa, W. Kucza, G. Cieślak, T. Kulik, M. Danielewski, J.-W. Yeh, Interdiffusion in the FCC-structured Al-Co-Cr-Fe-Ni high entropy alloys: experimental studies and numerical simulations, J. Alloys Compd. 674 (2016) 455–462.
[28] D. Gupta, Influence of solute Segregation on grain-boundary energy and self-diffusion, Metall. Trans. A 8 (9) (1977) 1431–1438.
[29] V.T. Borisov, V.M. Golikov, G.C. Shcherbedinskii, Connection between diffusion coefficients and energies of grain boundaries, Fiz. Met. Metalloved. 17 (1964) 881–885.
[30] M. Vaidya, K.G. Pradeep, B.S. Murty, G. Wilde, S.V. Divinski, Radioactive isotopes reveal a non sluggish kinetics of grain boundary diffusion in high entropy alloys, Sci. Rep. 7 (1) (2017) 12293.
[31] J.Y. He, H. Wang, Y. Wu, X.J. Liu, H.H. Mao, T.G. Nieh, Z.P. Lu, Precipitation behavior and its effects on tensile properties of FeCoNiCr high-entropy alloys, Intermetallics 79 (2016) 41–52.
[32] X.H. Du, W.P. Li, H.T. Chang, T. Yang, G.S. Duan, B.L. Wu, J.C. Huang, F.R. Chen, C.T. Liu, W.S. Chuang, Y. Lu, M.L. Sui, E.W. Huang, Dual heterogeneous structures lead to ultrahigh strength and uniform ductility in a Co-Cr-Ni medium-entropy alloy, Nat. Commun. 11 (1) (2020) 2390.
[33] S. Jiang, H. Wang, Y. Wu, X. Liu, H. Chen, M. Yao, B. Gault, D. Ponge, D. Raabe, A. Hirata, M. Chen, Y. Wang, Z. Lu, Ultrastrong steel via minimal lattice misfit and high-density nanoprecipitation, Nature 544 (7651) (2017) 460–464.
[34] X.-J. Ye, C.-S. Liu, W. Zhong, Y.-W. Du, Precipitate size dependence of Ni/Ni3Al interface energy, Phys. Lett. A 379 (1) (2015) 37–40.
[35] D. Williams, E. Butler, Grain boundary discontinuous precipitation reactions, Int. Met. Rev. 26 (1981) 153–183.
[36] Y.L. Sun, L.M. Fu, Z.Q. Fu, A.D. Shan, E.J. Lavernia, Enhanced thermal stability and ductility in a nanostructured Ni-based alloy, Scripta Mater. 141 (2017) 1–5.
[37] Y.H. Zhao, X.Z. Liao, S. Cheng, E. Ma, Y.T. Zhu, Simultaneously increasing the ductility and strength of nanostructured alloys, Adv. Mater. 18 (17) (2006) 2280–+.
[38] N. Tsuji, Y. Ito, Y. Saito, Y. Minamino, Strength and ductility of ultrafine grained aluminum and iron produced by ARB and annealing, Scripta Mater. 47 (12) (2002) 893–899.
[39] X.D. Xu, P. Liu, A. Hirata, S.X. Song, T.G. Nieh, M.W. Chen, Microstructural origins for a strong and ductile Al0.1CoCrFeNi high-entropy alloy with ultrafine grains, Materialia 4 (2018) 395–405.
[40] S.J. Sun, Y.Z. Tian, H.R. Lin, X.G. Dong, Y.H. Wang, Z.J. Zhang, Z.F. Zhang, Enhanced strength and ductility of bulk CoCrFeMnNi high entropy alloy having fully recrystallized ultrafine-grained structure, Mater. Des. 133 (2017) 122–127.
[41] S. Yoshida, T. Ikeuchi, T. Bhattacharjee, Y. Bai, A. Shibata, N. Tsuji, Effect of elemental combination on friction stress and Hall-Petch relationship in face-centered cubic high/medium entropy alloys, Acta Mater. 171 (2019) 201–215.
[42] M.A. Meyers, K.K. Chawla, Mechanical Behavior of Materials, Cambridge university press, 2008.
[43] R.L. Fleischer, Substitutional solution hardening, Acta Metall. 11 (3) (1963) 203–209.
[44] G. Williamson, S. Iii, Dislocation densities in some annealed and cold-worked metals from measurements on the X-ray debye-scherrer spectrum, Philos. Mag. A-Phys. Condens. Matter Struct. Defects Mechan. Properties - Phil. Mag. A 1 (1956) 34–46.
[45] W. Sylwestrowicz, E. Hall, The deformation and ageing of mild steel, Proc. Phys. Soc. Lond., Sect. B 64 (2002) 495.
[46] N. Petch, The cleavage strength of polycrystals, J. Iron Steel Inst. Lond. 173 (1953) 25.
[47] R. Cahn, Strengthening methods in crystals, Int. Mater. Rev. 17 (1972) 147, 147.
[48] C. Booth-Morrison, D.C. Dunand, D.N. Seidman, Coarsening resistance at 400°C of precipitation-strengthened Al–Zr–Sc–Er alloys, Acta Mater. 59 (18) (2011) 7029–7042.
[49] K. Ma, H. Wen, T. Hu, T. Topping, D. Isheim, D. Seidman, E. Lavernia, J. Schoenung, Mechanical behavior and strengthening mechanisms in ultrafine grain precipitation-strengthened aluminum alloy, Acta Mater. 62 (2014) 141–155.
[50] B. Gwalani, V. Soni, M. Lee, S.A. Mantri, Y. Ren, R. Banerjee, Optimizing the coupled effects of Hall-Petch and precipitation strengthening in a Al0.3CoCrFeNi high entropy alloy, Mater. Des. 121 (2017) 254–260.
[51] Z. Li, L. Fu, J. Peng, H. Zheng, X. Ji, Y. Sun, S. Ma, A. Shan, Improving mechanical properties of an FCC high-entropy alloy by γ' and B2 precipitates strengthening, Mater. Char. 159 (2020), 109989.
[52] C.-S. Kim, I. Sohn, M. Nezafati, J.B. Ferguson, B. Schultz, Z. Gohari Bajestani, P. Rohatgi, K. Cho, Prediction models for the yield strength of particle-reinforced unimodal pure magnesium (Mg) metal matrix nanocomposites (MMNCs), J. Mater. Sci. 48 (2013).